



**Flow Instability due to Coupling of Shear-Gradients to
Concentration:
Non-uniform flow of (hard-sphere) glasses**

Journal:	<i>Soft Matter</i>
Manuscript ID:	SM-ART-06-2014-001329.R1
Article Type:	Paper
Date Submitted by the Author:	28-Aug-2014
Complete List of Authors:	Jin, Howon; Seoul National University, School of Chemical and Biological Engineering Kang, Kyong; Forschungszentrum Juelich, ICS-3 Ahn, Kyung; Seoul National University, School of Chemical and Biological Engineering Dhont, Jan K G; Forschungszentrum Juelich, ICS-3; Heinrich-Heine University Duesseldorf, Department of Physics

Flow Instability due to Coupling of Shear-Gradients to Concentration: Non-uniform flow of (hard-sphere) glasses

Howon Jin^{1,2}, Kyongok Kang², Kyung Hyun Ahn¹, and Jan K.G. Dhont^{2,3}

¹ *Seoul National University
School of Chemical and Biological Engineering
Institute of Chemical Process
151-744 Seoul, Korea.*

² *Forschungszentrum Jülich
Institute of Complex Systems (ICS),
Soft Condensed Matter (ICS-3)
D-52425 Jülich, Germany.*

³ *Heinrich-Heine-Universität Düsseldorf
Department of Physics
D-40225 Düsseldorf, Germany.**

(Dated: August 29, 2014)

Flow-induced instabilities that lead to non-uniform stationary flow profiles have been observed in many different soft-matter systems. Two types of instabilities that lead to banded stationary states have been identified, which are commonly referred to as gradient- and vorticity-banding. The molecular origin of these instabilities is reasonably well understood. A third type of instability that has been proposed phenomenologically [Europhys. Lett., 1986, **2**, 129 and Phys. Rev. E, 1995, **52**, 4009] is largely unexplored. Essential to this "Shear-gradient Concentration Coupling" (SCC-) instability is a mass flux that is induced by spatial gradients of the shear rate. A possibly reason that this instability has essentially been ignored is that the molecular origin of the postulated mass flux is not clear, and no explicit expressions for the shear-rate and concentration dependence of the corresponding transport coefficient exist. It is therefore not yet known to what types of flow velocity- and concentration-profiles this instability gives rise to. In this paper, an expression for the transport coefficient corresponding to the shear-gradient induced mass flux is derived in terms of the shear-rate dependent pair-correlation function, and Brownian dynamics simulations for hard-spheres are presented that specify the shear-rate and concentration dependence of the pair-correlation function. This allows to explicitly formulate the coupled advection-diffusion equation and an equation of motion for the suspension flow velocity. The inclusion of a non-local contribution to the stress turns out to be essential to describe the SCC-banding transition. The coupled equations of motion are solved numerically, and flow- and concentration-profiles are discussed. It is shown that the SCC-instability occurs within the glass state at sufficiently small shear rates, leading to a banded flow-profile where one of the bands is non-flowing.

PACS numbers: 82.70.Dd, 64.70.Pf, 42.30.Va

I. INTRODUCTION

Shear-induced flow instabilities have been observed in a large variety of soft-matter systems. The most studied instability is the so-called *gradient-banding* instability, where in the stationary state typically two bands extending along the gradient direction are formed with different, spatially uniform shear rates. This type of

instability is observed, for example, in worm-like micellar systems, entangled polymeric systems, micellar cubic phases, transient networks, supra-molecular polymer solutions, liquid crystalline polymers, and surfactant solutions (the long list of references to this work can be found in overview papers in Refs.[1–8]). The gradient-banding instability is the result of a decreasing stress (of the homogeneously sheared suspension) with increasing shear rate. Any system that exhibits the very strong shear-thinning behaviour that is necessary to give rise to such a decrease of the stress will exhibit gradient banding. One of the earlier theories to describe this instability *assumed* the existence of an infinitely sharp interface between the bands, across which stress-boundary conditions were imposed [9, 10]. An approach in which the presence of interfaces between bands *naturally emerges* is to add a so-called stress-diffusion contribution to the equation of motion for the

*Electronic address: jinjin927@snu.ac.kr; Electronic address: k.kang@fz-juelich.de; Electronic address: ahnnet@snu.ac.kr; Electronic address: j.k.g.dhont@fz-juelich.de; URL: <http://plaza4.snu.ac.kr/~rheopro/?mid=Professor>; URL: http://www.fz-juelich.de/ICS/ICS-3/EN/Home/home_node.html

[72] † Electronic Supplementary Information (ESI) available: [Movies are available as supplementary material]. See DOI: [dx.doi.org/10.1039/c4sm00000x/](http://dx.doi.org/10.1039/c4sm00000x)

stress tensor [11–17]. The stress-diffusion contribution stabilizes the suspension against the very fast growth of arbitrary large gradients in the flow velocity. A somewhat different approach to describe the interface explicitly is to include a higher-order spatial derivative of the flow velocity in the standard expansion of the stress tensor, in order to account for large spatial gradients [6, 18]. This approach to account for the interface between shear bands will also be used in the present study. Gradient-banding kinetics and stress selection are affected by, for example, the dependence of the viscosity on concentration [29] and orientational order [19, 20], and the coupling of flow with the composition of binary mixtures where one of the components only exists under flow conditions [21]. A second relatively well understood instability is the so-called *vorticity-banding* instability, which leads to the formation of alternating bands which are stacked along the vorticity direction. It has been observed, for example, in systems of multi-lamellar vesicles, worm-like micelles, dispersions of rod-like colloids, nano-tube suspensions, and weakly aggregated colloidal suspensions (for references see the overview paper in Ref.[6]). There are several possible scenarios for the vorticity-banding instability, depending on the system under consideration. A possible mechanism underlying this instability is that hoop stresses are generated through the non-linear elastic deformation of the mesoscopic objects that are present in the dispersion [22], similar to the Weissenberg effect in polymeric systems. Instead of the non-linear elastic deformation of polymer chains, mesoscopic objects are now elastically deformed, like worm-like micelles, aggregates, or inhomogeneities formed during the initial stages of phase separation. Elastic instabilities have been discussed at length in Ref.[23]. Other scenario's for the formation of vorticity bands is that, after the formation of interfaces due to gradient-banding, the interface between the gradient-bands is unstable, where undulation of the interface subsequently leads to band-formation along the vorticity direction [24–26], or where the high shear-rate branch is unstable [27].

The molecular origins of the gradient-banding and vorticity-banding instabilities are thus quite different: gradient banding requires severe shear thinning of the shear viscosity and is thus driven by shear stresses, while the vorticity-banding instability is either an elastic instability leading to normal stresses, or is due to the instability of a gradient-banded interface or the high shear-rate branch. Coupling to concentration affects the gradient- and vorticity-banding kinetics and stationary states significantly, leading for example to an inclined shear-stress plateau and banding under controlled stress conditions [20, 28, 29]. However, concentration coupling is not the cause of these instabilities, contrary to the instability discussed in the present work. The instability discussed here is entirely due to concentration coupling, and does not occur without it. There

is a large body of literature concerned with the shear-flow induced enhancement of concentration fluctuations (see, for example, Refs.[30–35]), which might have a connection with the origin of the shear-induced instability of the sort discussed in the present paper [36].

Contrary to gradient- and vorticity-banding, very little attention has been given to this so-called *Shear-gradient Concentration Coupling (SCC-) instability*. This instability has been discussed by Nozieres and Quemada [37] and Schmitt et al. [38] within a phenomenological approach. An essential ingredient here is that a mass flux is induced by spatial gradients of the local shear rate. The origin of the shear-gradient induced mass flux is postulated in Refs.[37, 38] to be connected to an unspecified lift force or shear-rate dependent chemical potential, respectively. There are two subsequent studies on the SCC-instability, based on a irreversible thermodynamics approach where a shear-rate dependent chemical potential is again postulated [39], and a study on polymers, departing from the well-known Rolie-Poly constitutive model, where a square-gradient Ansatz for the mixing free energy is made [40]. All of these previous studies postulate either a shear-rate chemical potential or a osmotic pressure, and do not address the microscopic origin of the SCC-instability. The unexplained microscopic origin of the SCC-instability is probably the reason that this type of instability has hardly been pursued. To our knowledge there is only a single paper in which experiments on colloids are interpreted as being the result of the SCC-instability [41], where the driving force for the shear-gradient induced mass flux is formulated in terms of a shear-rate dependent osmotic pressure. Such a shear-rate dependent osmotic pressure has indeed been observed in experiments [42–44]. Brownian dynamics simulations on hard-sphere suspensions have been performed to quantify the shear-rate dependence of this generalized osmotic pressure [45]. Similar simulations in Ref.[46] relate to a mono-layer of colloids, where hydrodynamic interactions are at the origin of shear-gradient induced mass transport. The mechanism for shear-gradient induced mass fluxes proposed in Ref.[47, 48] is based on the assumption that the mass diffusion coefficient is shear-rate dependent, which gives rise to what is commonly known as "shear-induced diffusion". A diffusion equation is proposed that does not include an explicit contribution to the mass flux from gradients in the shear rate (see eq.(2.2) and the discussion in section 3 of Ref.[47]), contrary to the phenomenological approach by Schmitt et al. in Ref.[38]. This shear-induced diffusion leads to significant mass transport only for very large particles (larger than several tens of microns). It is important to note that the shear-gradient induced mass flux that is relevant for the SCC-instability is not of a hydrodynamic nature, and is not related to shear-induced diffusion, but is in essence due to direct inter-colloidal interactions.

In the present paper we discuss the microscopic origin of the shear-gradient induced mass flux due to direct inter-colloidal interactions in section II, which can be formulated in terms of a shear-rate dependent osmotic pressure. This leads to expressions for concentration and shear-rate dependent transport coefficients in terms of the shear-flow distorted pair-correlation function. Brownian dynamics simulations for hard-sphere suspensions are presented in section III, from which explicit expressions for these transport coefficients are obtained as functions of the concentration and shear-rate. This in turn allows to formulate the advection-diffusion equation, which couples to the Navier-Stokes equation, as discussed in section IV. Stability diagrams are constructed in section V on the basis of these equations of motion. The coupled advection-diffusion equation and the Navier-Stokes equation are solved numerically for a Couette geometry in section VI. An essential ingredient is a non-local contribution to the stress that accounts for stresses resulting from large gradients in the suspension flow velocity. This non-local contribution stabilizes the system against the unphysical arbitrary fast growth of large wave-vector Fourier components, and renders numerical algorithms stable. The resulting kinetics and stationary states are discussed in terms of flow-velocity profiles and concentration profiles.

II. THE ORIGIN OF THE SHEAR-GRADIENT CONCENTRATION COUPLING (SCC-) INSTABILITY

The self-amplifying mechanism that gives rise to the Shear-gradient Concentration Coupling (SCC-) instability can be understood intuitively as follows [6, 37, 41, 46, 49]. Consider a Couette cell, where the shear rate near the outer cylinder is smaller as compared to the inner cylinder. When a mass flux is induced by spatial gradients of the shear rate towards regions of smaller shear rates, mass will be transported towards the outer cylinder. The increase of concentration near the outer cylinder leads to an increase of the local stress. The response of the system is to decrease the stress by lowering the local shear rate. This amplifies spatial gradients of the shear rate, and leads to an enhanced mass flux towards the outer cylinder. The enhanced mass flux in turn gives rise to an even larger concentration, resulting in an even lower local shear rate. This is the self-amplifying mechanism that underlies the SCC-instability. A stationary state is reached once the diffusive mass flux due to existing concentration gradients cancels with the shear-gradient induced mass flux.

The SCC-instability may also occur in geometries where there are no deterministic, inherent gradients in the shear rate, like for a flat geometry. A fluctuation in the local flow velocity can also induce a mass flux that initiates the SCC self-amplifying mechanism. Such fluctua-

tions should be sufficiently long-lived in order that the necessary mass flux can develop to an extent that it becomes self-amplifying.

The SCC-instability has not been further analyzed after the original publications by Nozieres and Quemada [37] and by Schmitt [38], which is probably due to the ad-hoc introduction of a lift force and a shear-rate dependent chemical potential, respectively, of which the origin is uncertain. The aim of this section is to elucidate the origin of the shear-rate dependence of the relevant transport coefficients. A microscopic derivation of the mass flux from first principles will be discussed, and the origin of the shear-gradient contribution to the mass flux will be unambiguously identified. As will turn out, mass fluxes must be formulated in terms of a generalized osmotic pressure, as has been assumed in the analysis in Ref.[41]. This allows for the microscopic modeling of the advection-diffusion equation, including the mass flux induced by spatial gradients of the shear rate.

The driving force for mass transport induced by shear-gradients considered here is not to be confused with the phenomenon described in Refs.[47, 48]), where the mass flux is entirely described in terms of the shear-rate dependence of the Fickian diffusion coefficient. Here, no explicit shear-gradient contribution appears in the diffusion equation which is necessary for the SCC-instability. Mass transport for such "shear-induced diffusion processes" is only significant for large particles, and does not play a role in the SCC-instability as found in Ref.[41].

The general form of the diffusion-advection equation for the number density ρ of colloids, which undergoes a flow \mathbf{u} , reads (with the neglect of hydrodynamic interactions between the colloidal particles),

$$\frac{\partial \rho}{\partial t} + \nabla \cdot [\rho \mathbf{u}] = D_0 \nabla^2 \rho - \beta D_0 \nabla \cdot \mathbf{B}, \quad (1)$$

where $D_0 = k_B T / \xi_0$ is the free single-particle diffusion coefficient, with ξ_0 the friction coefficient, while interactions between colloidal particles are accounted for by the body force \mathbf{B} . The diffusion equation (1) complies with a continuity equation with a mass flux $\mathbf{j} = \rho \mathbf{v}$, where the thermally averaged velocity \mathbf{v} of a colloidal particle is equal to,

$$\mathbf{v} = \mathbf{u} + \frac{1}{\xi_0} \left[-k_B T \nabla \ln \rho + \frac{\mathbf{B}}{\rho} \right]. \quad (2)$$

This expresses force balance on the diffusive time scale, where the friction force $-\xi_0 \mathbf{v}$ balances with the Brownian force (the first term between the square brackets) and the body force \mathbf{B} which is due to colloid-colloid interactions. The body force that is due to direct inter-colloidal interactions is equal to,

$$\mathbf{B}(\mathbf{r}, t) = - \left\langle \sum_{i=1}^N [\nabla_i \Phi] \delta(\mathbf{r} - \mathbf{r}_i) \right\rangle, \quad (3)$$

with Φ the potential energy of an assembly of N colloidal particles, and where δ is the delta-distribution, with \mathbf{r}_i the position coordinate of colloid i .

The above general form of the diffusion equation is also given in Ref.[50], where the body force is referred to as "the particle contribution to the stress". The body force that includes forces on the colloidal particles *and* the solvent molecules is the body force that appears in the Navier-Stokes equation, and thus relates to the total stress.

We will now show how the expression (3) for the body force gives rise to a contribution in the mass flux that is proportional to $\nabla\dot{\gamma}$, where $\dot{\gamma}$ is the local shear rate. First of all, the ensemble average in eq.(3) is written in terms of an integral with respect to the probability density function P_N of the position coordinates of N spherical colloids,

$$\mathbf{B}(\mathbf{r}, t) = -N \int d\mathbf{r}_1 \cdots \int d\mathbf{r}_N P_N \nabla_1 \Phi \delta(\mathbf{r} - \mathbf{r}_1).$$

For a potential Φ that is a pair-wise additive sum of pair-interaction potentials V , it is readily found that,

$$\mathbf{B}(\mathbf{r}, t) = -N(N-1) \int d\mathbf{r}_2 P_2(\mathbf{r}, \mathbf{r}_2, t) \nabla V(|\mathbf{r} - \mathbf{r}_2|),$$

where,

$$P_2(\mathbf{r}_1, \mathbf{r}_2, t) = \int d\mathbf{r}_3 \cdots \int d\mathbf{r}_N P_N(\mathbf{r}_1, \mathbf{r}_2, \mathbf{r}_3, \cdots, \mathbf{r}_N, t).$$

Introducing the pair-correlation function g ,

$$P_2(\mathbf{r}, \mathbf{r}_2, t) = \frac{1}{N(N-1)} \rho(\mathbf{r}, t) \rho(\mathbf{r}_2, t) g(\mathbf{r}, \mathbf{r}_2, t, [\rho, \dot{\gamma}]),$$

where the notation $[\rho, \dot{\gamma}]$ is used to indicate functional dependence of the pair-correlation function on the density and shear rate (for the inhomogeneous systems under consideration), the body force on the colloidal particles can be written as,

$$\mathbf{B}(\mathbf{r}, t) = -\rho(\mathbf{r}, t) \int d\mathbf{r}_2 \rho(\mathbf{r}_2, t) g(\mathbf{r}, \mathbf{r}_2, t, [\rho, \dot{\gamma}]) \nabla V(|\mathbf{r} - \mathbf{r}_2|). \quad (4)$$

Since the potential restricts the integration range to distances $|\mathbf{r} - \mathbf{r}_2|$ less than the range R_V of the pair-interaction potential, only the short-ranged shear-induced distortion of the pair-correlation need be considered. For these small distances the shear-flow distortion of the pair-correlation function is to a good approximation affine, so that,

$$g(\mathbf{r}, \mathbf{r}_2, t, [\rho, \dot{\gamma}]) = g^{eq}(\mathbf{r}, \mathbf{r}_2, [\rho, \dot{\gamma}]) + g_0(\mathbf{r}, \mathbf{r}_2, t, [\rho, \dot{\gamma}]) + \frac{\mathbf{r} - \mathbf{r}_2}{|\mathbf{r} - \mathbf{r}_2|} \cdot \hat{\mathbf{E}} \cdot \frac{\mathbf{r} - \mathbf{r}_2}{|\mathbf{r} - \mathbf{r}_2|} g_1(\mathbf{r}, \mathbf{r}_2, t, [\rho, \dot{\gamma}]), \quad (5)$$

where g^{eq} is the equilibrium pair-correlation function in the absence of shear flow, g_0 is the isotropic shear-induced distortion, and g_1 characterizes the anisotropic affine distortion of the pair-correlation function. Furthermore, $\hat{\mathbf{E}}$ is the symmetric part of the velocity-gradient tensor divided by the local shear rate. As the expression (5) for the pair-correlation function assumes an affine distortion, this expression is accurate only when the Peclet number corresponding to the radius of the colloidal spheres is not larger than order unity. For a simple shear flow in the x -direction and with y the gradient direction, this tensor is equal to,

$$\hat{\mathbf{E}} = \frac{1}{2} \begin{pmatrix} 0 & 1 & 0 \\ 1 & 0 & 0 \\ 0 & 0 & 0 \end{pmatrix}.$$

The shear rate and colloid density vary only little over distances less than R_V , so that the density appearing in the integral (4) for the body force, $\rho(\mathbf{r}_2, t)$ can be Taylor expanded around \mathbf{r} to leading order in gradients,

$$\rho(\mathbf{r}_2, t) = \rho(\mathbf{r}, t) + (\mathbf{r}_2 - \mathbf{r}) \cdot \nabla \rho(\mathbf{r}, t). \quad (6)$$

For the same reason, the various contributions to the pair-correlation function in eq.(5) are approximately equal to those in a homogeneous system, with the density and shear rate taken in between the positions \mathbf{r} and \mathbf{r}_2 . For example,

$$g_0(\mathbf{r}, \mathbf{r}_2, t, [\rho, \dot{\gamma}]) = \bar{g}_0(|\mathbf{r} - \mathbf{r}_2|, \bar{\rho}, \bar{\dot{\gamma}}),$$

with $\bar{\rho} = \rho(\frac{1}{2}(\mathbf{r} + \mathbf{r}_2), t)$,
and $\bar{\dot{\gamma}} = \dot{\gamma}(\frac{1}{2}(\mathbf{r} + \mathbf{r}_2), t)$,

and similar for g^{eq} and g_1 . Here, the overbar on \bar{g}_0 is used to indicate that this is the correlation function of a homogeneous system with density $\bar{\rho}$ and shear rate $\bar{\dot{\gamma}}$. Since the temporal evolution of the long wave length density and shear rate variations are much slower than the relaxation time of the pair-correlation function for distances less than R_V , the pair-correlation function adjusts itself essentially instantaneously to its local stationary form. The time dependence of the pair-correlation function is therefore entirely due to the time dependence of the local density and shear rate. Within a leading order gradient expansion, we thus obtain ($\mathbf{R} = \mathbf{r}_2 - \mathbf{r}$),

$$g_0(|\mathbf{r} - \mathbf{r}_2|, t, [\rho, \dot{\gamma}]) = \bar{g}_0(R|\rho, \dot{\gamma}) + \frac{1}{2} \frac{\partial \bar{g}_0(R|\rho, \dot{\gamma})}{\partial \rho} \mathbf{R} \cdot \nabla \rho + \frac{1}{2} \frac{\partial \bar{g}_0(R|\rho, \dot{\gamma})}{\partial \dot{\gamma}} \mathbf{R} \cdot \nabla \dot{\gamma}, \quad (7)$$

and similar for g^{eq} (for which the shear-rate dependence is of course absent) and g_1 . Here, ρ and $\dot{\gamma}$ are now understood to denote the local density and shear rate (omitting the now superfluous overbar notation). Substitution of eqs.(6,7) into eq.(4) for \mathbf{B} , and performing

the angular integrations gives,

$$\mathbf{B}(\mathbf{r}, t) = - \left[\frac{\partial P_0(\rho, \dot{\gamma})}{\partial \rho} - k_B T \right] \nabla \rho - \frac{\partial P_0(\rho, \dot{\gamma})}{\partial \dot{\gamma}} \nabla \dot{\gamma} - \frac{\partial P_1(\rho, \dot{\gamma})}{\partial \rho} \hat{\mathbf{E}} \cdot \nabla \rho - \frac{\partial P_1(\rho, \dot{\gamma})}{\partial \dot{\gamma}} \hat{\mathbf{E}} \cdot \nabla \dot{\gamma}, \quad (8)$$

up to leading order in spatial gradients, where,

$$P_0(\rho, \dot{\gamma}) = \rho k_B T - \frac{2\pi}{3} \rho^2 \int_0^\infty dR R^3 \frac{dV(R)}{dR} [g^{eq}(R|\rho) + \bar{g}_0(R|\rho, \dot{\gamma})], \quad (9)$$

and,

$$P_1(\rho, \dot{\gamma}) = -\frac{4\pi}{15} \rho^2 \int_0^\infty dR R^3 \frac{dV(R)}{dR} \bar{g}_1(R|\rho, \dot{\gamma}).$$

Equation (8) can also be written as,

$$\mathbf{B}(\mathbf{r}, t) = -\nabla [P_0(\rho, \dot{\gamma}) - \rho k_B T] - \hat{\mathbf{E}} \cdot \nabla P_1(\rho, \dot{\gamma}), \quad (10)$$

where the gradient operators act on the spatial dependence of the colloid density and shear rate. The only component of the body force of interest here is the component acting along the gradient direction, which is the contribution $-\nabla [P_0 - \rho k_B T]$. According to eqs.(2,8) (with $\mathbf{j} = \rho \mathbf{v}$), the mass flux in the gradient direction is thus equal to,

$$\begin{aligned} \mathbf{j} &= \rho \mathbf{u} - \beta D_0 \nabla P_0(\rho, \dot{\gamma}) \\ &= \rho \mathbf{u} - \beta D_0 \left[\frac{\partial P_0(\rho, \dot{\gamma})}{\partial \rho} \nabla \rho + \frac{\partial P_0(\rho, \dot{\gamma})}{\partial \dot{\gamma}} \nabla \dot{\gamma} \right]. \end{aligned} \quad (11)$$

The interpretation of the above result for the mass flux is as follows. From equilibrium statistical mechanics, a well-known expression for the equilibrium pressure in terms of the pair-correlation function g^{eq} reads [51],

$$P^{eq}(\rho) = \rho k_B T - \frac{2\pi}{3} \rho^2 \int_0^\infty dR R^3 \frac{dV(R)}{dR} g^{eq}(R|\rho).$$

Since the correlation function relates to inter-colloidal interactions, this pressure is in fact the osmotic pressure [52]. This expression for the osmotic pressure is precisely the expression that we found for P_0 in eq.(9), except that the equilibrium pair-correlation function is now the shear-distorted pair-correlation function. This is why we shall refer to P_0 as a "generalized osmotic pressure". In this sense, just like for inhomogeneous unsheared systems, the mass flux is proportional to the spatial gradient of the osmotic pressure. The shear-rate dependence of this generalized osmotic pressure gives rise to the shear-gradient contribution to the mass flux. It should be noted that this generalized osmotic pressure is different from the pressure that appears in the Navier-Stokes equation. The pressure in the Navier-Stokes equation relates to the body force that includes

forces on both the colloids *and* the solvent molecules. The body force that appears in the advection-diffusion equation is the force that results from forces on the colloids only (see also the discussion in section III just below eq.(18)).

In the following we consider suspensions of hard spheres, for which the pair-interaction potential is either zero, when the cores do not overlap, or is infinite, when cores overlap. For such hard-core interactions the integral in eq.(9) for the generalized osmotic pressure can be evaluated in terms of the contact value of the pair-correlation function, that is, the value where the distance between two colloids is equal to $2a$, with a the radius of the cores. To this end the so-called cavity function $y = g \exp\{+\beta V\}$ is introduced (with $\beta = 1/k_B T$). This function is continuous at contact, and has the same contact value as the pair-correlation function [51]. Since $\exp\{-\beta V\} dV/dR = -k_B T d \exp\{-\beta V\}/dR = -k_B T \delta(R - 2a)$, with δ the delta-distribution, it follows from eq.(9) that,

$$P_0(\rho, \dot{\gamma}) = \rho k_B T + \frac{2\pi}{3} (2a)^3 \rho^2 k_B T g_{iso}^c(\rho, \dot{\gamma}), \quad (12)$$

where we abbreviated (the superscript "c" stands for "contact value"),

$$g_{iso}^c(\rho, \dot{\gamma}) = g^{eq}(R = 2a|\rho) + \bar{g}_0(R = 2a|\rho, \dot{\gamma}).$$

The body force along the gradient direction is, according to eqs.(10,12), therefore equal to,

$$\begin{aligned} \mathbf{B}(\mathbf{r}, t) &= \frac{2\pi}{3} (2a)^3 k_B T \frac{\partial \{ \rho^2 g_{iso}^c(\rho, \dot{\gamma}) \}}{\partial \rho} \nabla \rho \\ &+ \frac{2\pi}{3} (2a)^3 k_B T \rho^2 \frac{\partial g_{iso}^c(\rho, \dot{\gamma})}{\partial \dot{\gamma}} \nabla \dot{\gamma}. \end{aligned}$$

The mass flux in eq.(11) can now be most conveniently written as,

$$\mathbf{j} = \rho \mathbf{u} - D_{eff} \nabla \rho - \xi \nabla \dot{\gamma}, \quad (13)$$

where the *effective diffusion coefficient* is equal to,

$$D_{eff}(\rho, \dot{\gamma}) = D_0 \left[1 + \frac{2\pi}{3} (2a)^3 \frac{\partial \{ \rho^2 g_{iso}^c(\rho, \dot{\gamma}) \}}{\partial \rho} \right], \quad (14)$$

and the *shear-gradient coefficient* is equal to,

$$\xi(\rho, \dot{\gamma}) = D_0 \frac{2\pi}{3} (2a)^3 \rho^2 \frac{\partial g_{iso}^c(\rho, \dot{\gamma})}{\partial \dot{\gamma}}. \quad (15)$$

The explicit density and shear-rate dependence of these transport coefficients will be obtained by means of Brownian dynamics simulations, from which the contact values of the pair-correlation function are obtained, which then allows to analyze the transient kinetics and stationary states resulting from the SCC-instability.

III. BROWNIAN DYNAMICS SIMULATIONS

In this section, Brownian dynamics (BD-) simulations are presented, in order to determine the concentration and shear-rate dependence of the contact value of the pair-correlation function under shear flow conditions. The simulation results will be used to establish the explicit concentration and shear-rate dependence of the effective diffusion coefficient (14) and the shear-gradient coefficient (15).

The governing equation for BD-simulations is the overdamped Langevin equation,

$$\mathbf{0} = \mathbf{F}_i^H + \mathbf{F}_i^P + \mathbf{F}_i^B ,$$

where \mathbf{F}_i^H , \mathbf{F}_i^P and \mathbf{F}_i^B are the hydrodynamic force, the inter-particle force, and the Brownian force exerted on the i^{th} particle, respectively. On the diffusive time scale under consideration, inertial forces can be ignored. With the neglect of hydrodynamic interactions between the colloids, the hydrodynamic force is equal to,

$$\mathbf{F}_i^H = \xi_0 (\mathbf{v}_i - \mathbf{u}_i) ,$$

where $\xi_0 = 6\pi\eta_0 a$ is the single-particle friction coefficient (with η_0 the shear viscosity of the solvent, and a the radius of the spheres), \mathbf{v}_i is the velocity of the sphere, and \mathbf{u}_i the externally imposed solvent velocity at the position of the sphere. For the inter-particle force \mathbf{F}_i^P , we employ the overlap-preventing potential free method [45, 53]. Here, after a move of the particles leading to core-overlap, they are forced to move back to a position where there is contact between the surfaces. The corresponding displacement is equal to (with \mathbf{r}_{ij} the vector connecting the two centers of the overlapping spheres),

$$\Delta\mathbf{r}_i^{overlap} = \frac{1}{2} \frac{\mathbf{r}_{ij}}{r_{ij}} (r_{ij} - 2a) \quad , \quad r_{ij} < 2a .$$

The Brownian force \mathbf{F}_i^B is generated as a random number, with zero average and variance complying to the equipartition of kinetic energy,

$$\begin{aligned} \langle \mathbf{F}_i^B \rangle &= \mathbf{0} , \\ \langle \mathbf{F}_i^B(t) \mathbf{F}_i^B(t') \rangle &= 2\xi_0 k_B T \hat{\mathbf{I}} \delta(t - t') , \end{aligned}$$

where $\hat{\mathbf{I}}$ is the identity tensor.

Introducing dimensionless variables by rescaling length with the radius a , energy with $k_B T$, and time with a^2/D_0 (the time required for a particle to diffuse over a distance equal to its own radius), the dimensionless displacement of the position of particle i is (the overtilde is used to indicate dimensionless variables),

$$d\tilde{\mathbf{r}}_i = \left[\tilde{\mathbf{v}}_i^\infty + \tilde{\mathbf{F}}_i^P \right] d\tilde{t} + \sqrt{2} d\tilde{\mathbf{W}}_i , \quad (16)$$

where,

$$\tilde{\mathbf{F}}_i^P = \Delta\tilde{\mathbf{r}}_i^{overlap} / d\tilde{t} ,$$

and where $d\tilde{\mathbf{W}}_i$ is the random dimensionless displacement due to the Brownian force, such that,

$$\begin{aligned} \langle d\tilde{\mathbf{W}}_i \rangle &= \mathbf{0} , \\ \langle d\tilde{\mathbf{W}}_i(t) d\tilde{\mathbf{W}}_i(t') \rangle &= \hat{\mathbf{I}} \delta(t - t') dt . \end{aligned}$$

Furthermore, the dimensionless imposed solvent velocity $\tilde{\mathbf{v}}_i^\infty = \tilde{\mathbf{\Gamma}} \cdot \tilde{\mathbf{r}}_i$, where the dimensionless velocity gradient tensor $\tilde{\mathbf{\Gamma}}$ has only one non-zero component, the xy element, which is equal to the Peclet number,

$$Pe = \tilde{\gamma} = \dot{\gamma} a^2 / D_0 .$$

Time integration of eq.(16) extends over the interval $\tilde{t} = 0 - 100$ with time-steps of $d\tilde{t} = 10^{-4}$, for shear rates in the range $\tilde{\gamma} = 0.01 - 10$ and for volume fractions ranging from 0.25 to 0.55. In this concentration and shear-rate range there is no SCC-instability, and crystallization is not observed (probably because nucleation requires larger systems and/or it is too slow on the time scale during which the simulations are performed). We used a box containing $N = 3375$ particles with periodic boundary conditions. **We verified that this number of particles is sufficiently large, by repeating simulations with 1000 particles, leading to results that are the same to within 2%.**

After the steady state is reached, the pair-correlation function $g(\mathbf{r})$ is calculated from,

$$g(\mathbf{r}) = \frac{1}{\bar{\rho}^2} \left\langle \sum_{i=1}^N \sum_{\substack{j=1 \\ j \neq i}}^N \delta(\mathbf{r} - \mathbf{r}_{ij}) \right\rangle ,$$

where $\bar{\rho}$ is average number density of particles, and the brackets denote time-averaging. An accurate description of the contact value of the pair-correlation function for hard spheres without shear flow up to concentrations of about 45 % is given by the so-called Carnahan-Starling equation [54],

$$g^{eq,c}(\phi) = \frac{2 - \phi}{2(1 - \phi)^3} , \quad (17)$$

where,

$$\phi = \frac{4\pi}{3} a^3 \rho ,$$

is the dimensionless concentration: the volume fraction of colloidal spheres. A comparison of our BD-equilibrium simulation results with the Carnahan-Starling equation is shown in Fig.1. There is a reasonable agreement, with small deviations at very high

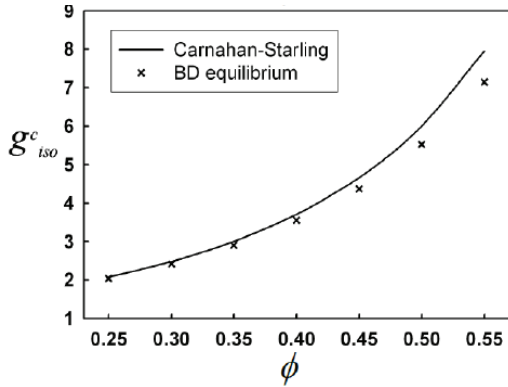


FIG. 1: A comparison between the simulated contact values of the equilibrium pair-correlation function (the data points) and the Carnahan-Starling equation (17) (the solid line).

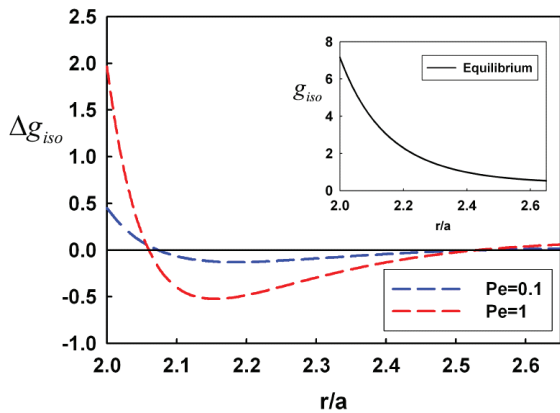


FIG. 2: The difference Δg between the angular averaged pair-correlation function and the equilibrium pair-correlation function as a function of the inter-particle separation in units of the particle radius a . The inset shows the equilibrium pair-correlation function. The volume fraction is 55 %.

volume fractions above 45 %, similar to what is found in Ref.[45]. This slight overestimation is attributed in Ref.[45] to the effective softness that is introduced in the simulations through unresolved particle overlaps.

Of interest for the calculation of the transport coefficients in eqs.(14,15) is the contact value of the isotropic part of the pair-correlation function, which according to eq.(5), is equal to the angular-averaged pair-correlation function at the core surface,

$$g_{iso}(R) = g^{eq}(R|\rho) + \bar{g}_0(R|\rho, \dot{\gamma}) = \frac{1}{4\pi} \oint d\hat{\mathbf{r}} g(\mathbf{r}),$$

where the integral ranges over the directions of \mathbf{r} . Examples of the isotropic part of shear-distorted pair-correlation function are plotted as a function of the inter-particle separation for two shear rates in Fig.2.

An example of the effect of shear flow on the pair-

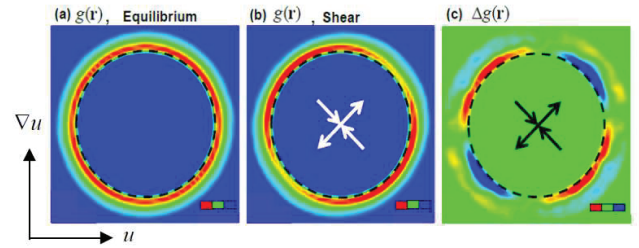


FIG. 3: (a) The pair correlation function for a volume fraction of 45 % in equilibrium, without shear flow. The colour code indicates the value of the pair-correlation function (blue is a low value, red a high value). (b) Same as in (a), but now for a shear rate corresponding to a Peclet number equal to $\tilde{\gamma} = 0.5$. The arrows indicate the compressional and extensional directions. (c) The difference between the pair-correlation functions under shear in (b) and without shear in (a). The blue colour code now corresponds to a negative value, red to a positive value.

correlation function is shown in Fig.3, for a volume fraction of 45 %. In Fig.3a the pair-correlation function without shear flow is shown, where the colour code measures the value of the correlation function (blue is a low value, red a high value). The dotted circle indicates the location of the core-surface. In Fig.3b the pair-correlation in shear flow is plotted, and in Fig.3c the difference between pair-correlation function under flow and its equilibrium value is shown. There is a pronounced increase of the pair-correlation function along the compressional direction, and a clear decrease along the extensional axis, as expected. We note that the shear-induced stripes and peaks exhibit by the pair-correlation function as found in Ref.[45] only occurs at Peclet numbers larger than about 10. Here, the analysis is restricted to Peclet numbers less than 1, for which the same oval structure for the pair-correlation function as seen in Fig.3 is also found in Ref.[45]. The difference Δg_{iso} between the angular averaged pair-correlation function and the equilibrium pair-correlation function is given in Fig.2 as a function of the inter-particle separation, for two Peclet numbers. As can be seen, the contact value is a strong function of the shear rate.

Concentration and shear-rate dependent contact values of the isotropic part of the pair-correlation function are shown in Fig.4a, where the data points are BD-simulation results for various volume fractions. As can be seen from Fig.4b, the shear-distorted part $\Delta g_{iso}^c = g_{iso}^c - g^{eq,c}$ of the isotropic contact value of the pair-correlation function varies like $\sim \tilde{\gamma}^m$ for each volume fraction. The volume fraction dependence of m is shown in Fig.4c, where the solid line corresponds to,

$$m = 0.43 + 5.26\phi - 8.80\phi^2. \quad (18)$$

Note that, according to eqs.(12,19,20), the osmotic pressure varies like $\sim \tilde{\gamma}^m$, where the Peclet number is to be

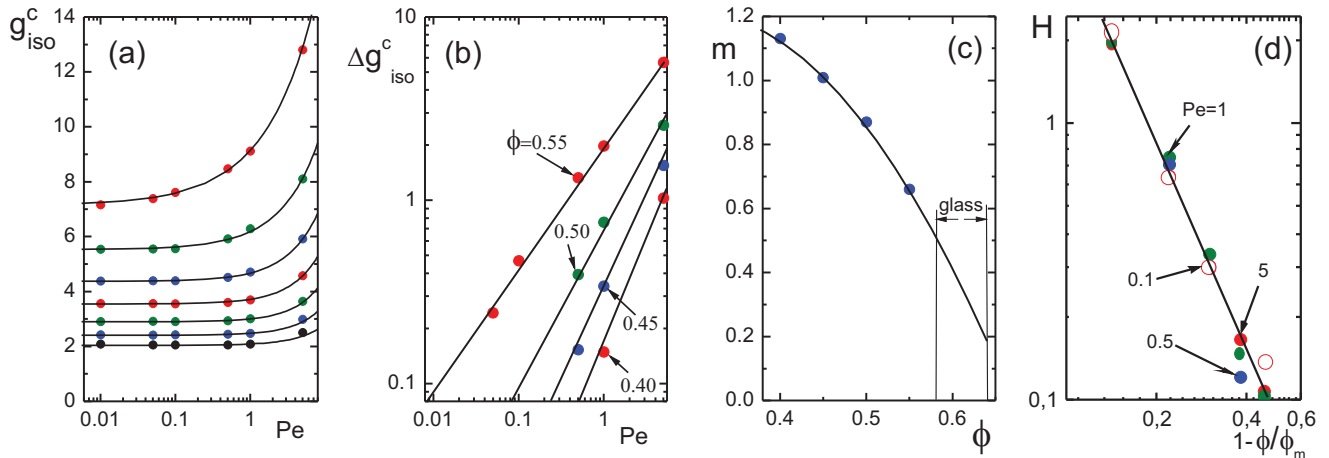


FIG. 4: (a) The contact value g_{iso}^c of the isotropic part of the pair-correlation function as a function of the Peclet number for various volume fractions. The data points are BD-simulation results for $\phi = 0.25$ (the lower set of data points) up to 0.55 (the upper set of data points), increasing in steps of 0.05. (b) The difference Δg_{iso}^c between the isotropic contact values of the pair-correlation function of the sheared and unsheared equilibrium system as a function of the Peclet number for various volume fractions. The slope of the straight lines in this double-logarithmic plot is equal to the exponent m in eq.(19). (c) The exponent m as a function of the volume fraction. The solid curve is the second order polynomial in eq.(18). (d) The quantity $H \equiv \Delta g_{iso}^c / \tilde{\gamma}^m$ as a function of $1 - \phi/\phi_m$ on a double-logarithmic scale. The slope of the straight line is equal to the exponent $-s$ in eq.(19). Some of the data points fall right on top of each other, so that they are not visible in this plot.

interpreted as its absolute value, since reversal of the shear rate does not change the osmotic pressure. An approximate linear dependence of the shear-induced osmotic pressure on the applied shear rate is found experimentally in Ref.[44] for volume fractions ranging from 0.30 to 0.50 (see in particular their Fig.3). The exponent m is indeed found in Fig.4c to be close to unity within this range of volume fractions. As hydrodynamic interactions are neglected in our BD-simulations, it thus seems that the functional shear-rate dependence is not too much affected by such hydrodynamic intercolloidal interactions. It should be mentioned, however, that the Peclet numbers in Ref.[44] is extremely high, so that the agreement between our results and those experiments may be fortuitous. A linear dependence of the osmotic pressure on the shear rate for concentrations below ϕ_g has also been proposed in Ref.[46] (see, for example, their eq.(39)). Brownian dynamics simulations have been performed in Ref.[45], likewise with the neglect of hydrodynamic interactions, where it is found that the pressure as obtained from the trace of the stress tensor corresponds to $m \approx 1.7$ for a volume fraction of 0.45 and for Peclet numbers ranging from 0.1 to 1 (see their Fig.17). As the body force in the advection-diffusion equation accounts for forces on the colloidal particles only, while the pressure obtained from the trace of the stress tensor includes in addition the forces on the solvent, the osmotic pressure discussed

in the present paper is different from that in Ref.[45]. Gradients in the osmotic pressure as considered here lead to *diffusive* mass transport, while the pressure appearing in the Navier-Stokes equation in Ref.[45] leads to *convective* transport. This is the reason why a different exponent of 1.7 is reported in Ref.[45] as compared to our results.

As a glass is a "frozen-in liquid", microstructural order in the quiescent glass state is very similar to that in a fluid. This is most probably the reason why molecular dynamics simulations on hard-sphere systems find that the contact value of the pair-correlation function (without shear flow) changes smoothly from the fluid, to the meta-stable fluid region, to the glass state, on increasing the concentration [55]. This also underlies the assumption in mode coupling theory that extrapolated structurefactors from fluids to concentrations within the glass state can be used to assess glassy dynamics. As yet, however, there are no rigorous arguments for smooth variations of structural variables from (meta-stable) fluids into the glassy state, not for unsheared and not for sheared systems. We assume here that the same smooth variations as seen in simulations and often assumed for unsheared systems also holds for sheared systems. As long as no crystallization occurs, the flowing branch of a glass most probably behaves very much like a concentrated flowing fluid. The concentration dependence of m within the fluid state is thus smoothly

extrapolated into the glass state as shown in Fig.4c.

In Fig.4d the quantity $H \equiv \Delta g_{iso}^c / \tilde{\gamma}^m$ is seen to vary like $\sim (1 - \phi/\phi_m)^{-s}$, where $\phi_m = 0.64$ is the maximum random close packing volume fraction of spheres, and with,

$$s = 2.525 ,$$

independent of the shear rate. Furthermore, H is found to be independent of the shear rate. These results imply that,

$$g_{iso}^c(\phi, \tilde{\gamma}) = g^{eq, c}(\phi) + A \tilde{\gamma}^m \left(1 - \frac{\phi}{\phi_m}\right)^{-s} , \quad (19)$$

is an accurate representation of the contact value of the isotropic part of the pair-correlation function. The value of the amplitude A is found to be equal to,

$$A = 0.0140 .$$

The solid lines in Fig.4a correspond to the representation (19), which is indeed seen to describe the BD-simulation data perfectly.

The expression (19) for the pair-correlation function specify the shear-rate and volume fraction dependencies of the transport coefficients in eqs.(14,15), which will be solved numerically for a Couette geometry in section VI.

IV. EQUATIONS OF MOTION

Brownian dynamics simulations can not be used to analyze the SCC-instability, since unrealistically large systems must be simulated to achieve this. Instead, equations of motion must be formulated which are then solved numerically. In this section we will formulate the two necessary equations of motion. In subsection IV A we will state the advection-diffusion equation as obtained from the considerations in the previous sections, and in subsection IV B the equation of motion for the flow velocity is discussed.

A. The advection-diffusion equation

The advection-diffusion equation as derived in section II does not assume equilibrium, and is therefore also applicable within the glass state. In addition, since microstructural order in the glass is very similar to that in the fluid, the contact value (19) for the pair-correlation function is expected to be reasonable also within the glass. The advection-diffusion equation, applicable to fluids and glasses, thus follows immediately from eqs.(13,14,15),

$$\frac{\partial \rho}{\partial t} + \nabla \cdot [\rho \mathbf{u}] = \nabla \cdot [D_{eff} \nabla \rho] + \nabla \cdot [\xi \nabla \dot{\gamma}] , \quad (20)$$

where \mathbf{u} is the suspension flow velocity, the effective diffusion coefficient in terms of dimensionless variables is equal to,

$$D_{eff}(\phi, \tilde{\gamma}) = D_0 \left[1 + 4 \frac{\partial}{\partial \phi} \left\{ \phi^2 g_{iso}^c(\phi, \tilde{\gamma}) \right\} \right] ,$$

and the shear-gradient coefficient is equal to,

$$\xi(\phi, \tilde{\gamma}) = 18 \eta_0 \frac{D_0}{k_B T} \phi^2 \frac{\partial g_{iso}^c(\phi, \tilde{\gamma})}{\partial \tilde{\gamma}} .$$

The concentration and shear-rate dependence of the contact value g_{iso}^c of the isotropic part of the pair-correlation function is specified by eq.(19), as obtained from the BD-simulations.

As mentioned before, the shear-rate induced mass flux as described in Ref.[47] is entirely assumed to be due to the shear-rate dependence of D_{eff} in eq.(20) [48]. This so-called shear-induced diffusion leads to significant mass transport only for very large particles, larger than several tens of microns. There is no SCC-instability without the explicit contribution from shear-gradient induced mass transport.

Our equation of motion (20) is coupled to the equation of motion for the suspension flow velocity \mathbf{u} , which is discussed in the next subsection.

B. The equation of motion for the suspension flow velocity

Although the rheological properties of concentrated hard-sphere suspensions could in principle be obtained from similar Brownian Dynamics simulations as discussed in section III, there is an abundance of literature on simulations and rheological experiments of hard-sphere systems available to be able to construct a reliable Navier-Stokes equation. We chose to use this existing information to construct the Navier-Stokes equation, rather than to perform a separate Brownian Dynamics study, which would merely reproduce existing knowledge.

The inertial contribution to the Navier-Stokes equations can be neglected for the low Reynolds numbers typical for colloidal systems. Furthermore, the relaxation of the fluid velocity is very fast in comparison to the temporal evolution of the colloid concentration, which can be seen as follows. The time τ_{sw} that a shear wave needs to traverse a distance l is equal to $\rho_m l^2 / \eta$ (with ρ_m the specific mass density of the suspension). A lower bound for the time needed for the colloid concentration to change over a length scale l is the time $\tau_{diff} = l^2 / D_{eff}$ needed for a colloidal sphere to diffuse over that distance. When the ratio $\tau_{diff} / \tau_{sw} = \eta / (\rho_m D_{eff})$ is large, the flow velocity is enslaved by colloid concentration. Substitution of typical numbers (shear viscosity 10^{-2} N s/m^2 , mass density

10^3 kg/m^3 , and diffusion coefficient $10^{-11} \text{ m}^2/\text{s}$) shows that this ratio is of the order 10^6 . This validates the assumption that flow is enslaved by concentration, so that the explicit time derivative in the Navier-Stokes equation can be neglected. The Navier-Stokes equation therefore reduces to,

$$\mathbf{0} = \nabla \cdot \boldsymbol{\Sigma} , \quad (21)$$

where $\boldsymbol{\Sigma}$ is stress tensor. The standard expression for the stress tensor is $\boldsymbol{\Sigma} = \boldsymbol{\Sigma}_{yield} + \eta [\nabla \mathbf{u} + (\nabla \mathbf{u})^T]$ ("T" stands for "transposition"), where $\boldsymbol{\Sigma}_{yield}$ is the yield-stress tensor, which is zero below the glass-transition volume fraction $\phi_g = 0.58$, and where η is the shear-viscosity. Spatial variations in the pressure are absent for the flow profiles under consideration here, which are therefore omitted. This expression for the stress tensor is the result of a leading order expansion with respect to gradients in the flow velocity \mathbf{u} . In banded profiles, however, gradients may be large, so that the next higher order term in such a gradient expansion must be included. This non-local contribution to the stress turns out to be essential to be able to describe the formation of banded flow profiles, as it stabilizes the system against the arbitrary fast growth of large gradients in the flow velocity (this is shown in the linear stability analysis in section V). This holds for gradient-banding as well as for the SCC-instability. The total stress tensor is therefore equal to [18],

$$\boldsymbol{\Sigma} = \boldsymbol{\Sigma}_{yield} + (\eta - \kappa \nabla^2) [\nabla \mathbf{u} + (\nabla \mathbf{u})^T] , \quad (22)$$

where $\kappa > 0$ is referred to as the *shear-curvature viscosity*. Both η and κ are functions of the concentration and shear rate, which is essentially different below and above the glass concentration.

What has been neglected in the constitutive relation in eq.(22) are normal stresses. As we restrict ourselves to laminar flow within symmetric geometries like a Couette cell or parallel plates, and spatial gradients of the shear rate are essential for the SCC instability, we neglect these normal stresses. For flows in more complex geometries, where normal stresses affect the direction of flow velocities, and thereby spatial gradients in the shear rate, a more realistic constitutive relation should be employed that includes normal stresses.

For volume fractions $\phi < \phi_g$ there is a Newtonian plateau up to Peclet numbers of approximately 0.1 to 1 up to volume fraction close to ϕ_g [45, 56–61], in agreement with the simulation data in Fig.4a. For values of Peclet numbers smaller than unity that are of interest here, within the Newtonian plateau, the viscosity in eq.(22) is thus approximated by the zero-shear viscosity. There are several propositions that describe the concentration dependence for the viscosity of hard-sphere suspensions quite accurately, like an exponential dependence on concentration [62] and through generalized Stokes-Einstein relations [63, 64]). Here we use the

well-known Krieger-Dougherty relation [65],

$$\eta(\phi, \tilde{\gamma}) = \eta_0 (1 - \Phi)^{-q} , \quad \phi < \phi_g ,$$

for the concentration dependence of the zero-shear viscosity, where η_0 is solvent viscosity, and where the notation,

$$\Phi = \phi/\phi_m .$$

is adopted from Ref.[41] as a dimensionless concentration. The experimental values of q that are reported vary from $2.5 \times \phi_m = 1.6$ [57] to 2 [58], up to concentrations of about 0.59. A theory for barrier formation and particle hopping predicts an exponent of 9.1 in the concentration range of 0.505–0.605 [66]. We adopt here the value,

$$q = 2 ,$$

which describes experimental data on hard-sphere silica dispersions quite accurately. The shear-curvature viscosity diverges similarly as the viscosity at the volume fraction ϕ_m , while the range of shear rates where shear thinning occurs is similar for both [18]. We will therefore assume the same concentration dependence for the shear-curvature viscosity as for the shear viscosity,

$$\kappa(\phi, \tilde{\gamma}) = \kappa_0 (1 - \Phi)^{-q} , \quad \phi < \phi_g .$$

where κ_0 is a constant.

Contrary to fluid suspensions, there is no Newtonian plateau in hard-sphere glasses. Shear thinning immediately sets in when flow is induced by applying a stress just above the yield stress, which is reasonably well described by a Herschel-Bulkley form of the stress, which predicts that the viscosity in eq.(22) varies like $\sim \tilde{\gamma}^{-1/2}$ [41, 67, 68]. We therefore adopt the same Herschel-Bulkley form as used in Ref.[41] (see their eq.(4) with $p = 3$, $n = 0.5$, and $A = 15$),

$$\eta(\phi, \tilde{\gamma}) = 15 \frac{a^2}{D_0} \Sigma_{yield}(\Phi) (1 - \Phi)^{1/2} \tilde{\gamma}^{-1/2} , \quad \phi > \phi_g .$$

The concentration dependence of the yield stress of hard-sphere glasses is $\sim (1 - \Phi)^{-p}$, where p is reported to vary between 1 and 3, while the prefactor is equal to $k_B T / (100a^3)$ [41, 69]. We will use the same expression for the yield stress as in Ref.[41],

$$\Sigma_{yield} = \frac{k_B T}{100 a^3} (1 - \Phi)^{-p} , \quad (23)$$

which is understood to act along the flow direction. The exponent is equal to,

$$p = 3 .$$

The shear-curvature viscosity has again a similar shear-rate and concentration dependence as the shear viscosity,

$$\kappa(\phi, \dot{\gamma}) = 15 \frac{a^2}{D_0} \frac{\kappa_0}{\eta_0} \Sigma_{yield}(\Phi) (1 - \Phi)^{1/2} \dot{\gamma}^{-1/2}, \quad \phi > \phi_g.$$

Note that the apparent divergence of the viscosity at zero shear rate is of no concern as only the stress enters the Navier-Stokes equation, which is well-behaved at zero shear rates (and varies like $\sim \dot{\gamma}^{-1/2}$).

V. LINEAR STABILITY ANALYSIS AND THE STABILITY DIAGRAM

The linear stability analysis given in previous work on the SCC-instability of colloids could only be done for zero wave vectors, since the non-local contribution, as quantified by the shear-curvature viscosity, has not been included before. Without this contribution, the growth rate of variations/fluctuations of the flow velocity indefinitely increases with increasing wave vectors, which is unphysical. The non-local contribution renders variations/fluctuations of sufficiently large wave vectors stable, which is required to derive a physically meaningful dispersion relation.

Consider a flow in the x -direction with gradients in density and flow velocity only the y -direction. Within the glass, the applied shear stress is supposed to be larger than the yield stress. Substitution of $\rho = \rho_0 + \delta\rho$ and $u = \dot{\gamma}_0 y + \delta u$ into the advection-diffusion equation, where ρ_0 and $\dot{\gamma}_0$ are the constant initial density and shear rate respectively, and linearization with respect to the small perturbations $\delta\rho$ and δu gives,

$$\frac{\partial \delta\rho}{\partial t} = D_{eff} \frac{\partial^2 \delta\rho}{\partial y^2} + \xi \frac{\partial^3 \delta u}{\partial y^3}, \quad (24)$$

where D_{eff} and ξ are understood to be evaluated at the density ρ_0 and shear rate $\dot{\gamma}_0$. The equation of motion for the flow velocity similarly gives,

$$0 = \frac{\partial \sigma}{\partial \dot{\gamma}_0} \frac{\partial^2 \delta u}{\partial y^2} + \frac{\partial \sigma}{\partial \rho_0} \frac{\partial \delta\rho}{\partial y} - \kappa \frac{\partial^4 \delta u}{\partial y^4}. \quad (25)$$

where η and κ are evaluated at ρ_0 and $\dot{\gamma}_0$, and where,

$$\begin{aligned} \sigma &= \dot{\gamma}_0 \eta(\rho_0, \dot{\gamma}_0) & , & \quad \phi < \phi_g, \\ \sigma &= \Sigma_{yield}(\rho_0) + \dot{\gamma}_0 \eta(\rho_0, \dot{\gamma}_0) & , & \quad \phi \geq \phi_g, \end{aligned}$$

is the shear-stress of the initially homogeneously sheared suspension, again at the density ρ_0 and the shear rate $\dot{\gamma}_0$. The time dependence of the perturbations will be exponential due to the linearization. The exponents for the density and flow velocity are the same,

as the velocity is enslaved by the concentration. Hence, for sinusoidal spatial perturbations,

$$\begin{aligned} \delta\rho &= \delta\rho_0 \exp\{iky - \lambda(k)t\}, \\ \delta u &= \delta u_0 \exp\{iky - \lambda(k)t\}. \end{aligned} \quad (26)$$

Substitution into eqs.(24,25) leads to the dispersion relation,

$$\lambda(k) = k^2 \left[D_{eff} - \xi \frac{d\sigma}{d\rho} \left\{ \frac{d\sigma}{d\dot{\gamma}} + \kappa k^2 \right\}^{-1} \right]. \quad (27)$$

According to eq.(26), the initial density and flow profiles are unstable when $\lambda < 0$, that is, when,

$$D_{eff} \left(\frac{d\sigma}{d\dot{\gamma}} + \kappa k^2 \right) < \xi \frac{d\sigma}{d\rho} \rightarrow \text{unstable}. \quad (28)$$

Since $\kappa > 0$, this result shows that perturbations corresponding to large spatial gradients, for which the corresponding wave vector k is large, are stable. Only sufficiently smooth variations in density and shear rate will be unstable, while rapidly varying variations remain stable. It thus follows from eq.(28) that the system is unstable against arbitrary smooth spatially varying perturbations (for which $k = 0$), when the *stability factor*,

$$S \equiv \frac{\xi}{D_{eff}} \frac{d\sigma/d\rho}{d\sigma/d\dot{\gamma}}, \quad (29)$$

is larger than unity. This reproduces the SCC-stability criterion as derived similarly in Refs.[37, 38, 41].

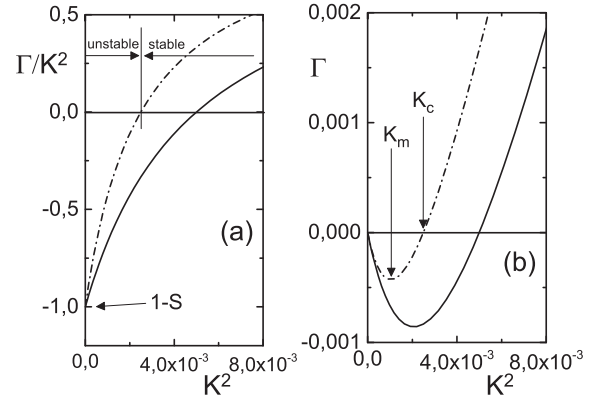


FIG. 5: (a) The dimensionless quantity Γ/K^2 , and (b) the dimensionless (negative) growth rate Γ as a function of the squared dimensionless wave vector $K = ka$. Here, $S = 2$ and $C = 200$ (solid curves) and $C = 400$ (dashed-dotted lines).

The dispersion relation (27) is most conveniently written in dimensionless form as,

$$\Gamma = K^2 \left[1 - \frac{S}{1 + CK^2} \right],$$

where $\Gamma = \lambda(k) a^2 / D_{eff}$ is the dimensionless (negative) growth rate, $K = k a$ is the dimensionless wave vector (with a the radius of the colloidal spheres), S is again the stability factor in eq.(29), and $C = \kappa / (a^2 d\sigma/d\dot{\gamma})$. The quantity Γ/K^2 is plotted in Fig.5a as a function of K^2 for the typical values of $S = 2$ and $C = 200$ (solid curve) and $C = 400$ (dashed-dotted curve). Those wave vectors where $\Gamma < 0$ are unstable, while larger wave vectors corresponding to large spatial gradients remain stable. The fastest growing Fourier mode is the mode where Γ attains its minimum in Fig.5b. The stabilization of Fourier modes with large wave vectors is solely due to the non-local stress contribution as characterized by the shear-curvature viscosity κ . As can be seen, the larger the shear-curvature viscosity (to which C is proportional to), the smaller the wave-vector range where the system is unstable. For $\kappa = 0$ the growth rate increases indefinitely like $\sim K^2$ with increasing wave vector. Such an arbitrary fast growth of large spatial gradients is unphysical.

The critical wave vector k_c beyond which spatial variations are stable, for which $\lambda(k) = 0$, follows from eq.(28) as,

$$k_c = \sqrt{\frac{d\sigma/d\dot{\gamma}}{\kappa}} (S - 1) \quad , \quad (S > 1) \quad , \quad (30)$$

while the fastest growing Fourier mode is the one with the wave vector k_m for which $d\lambda/dk = 0$, and hence,

$$k_m = \sqrt{\frac{d\sigma/d\dot{\gamma}}{\kappa}} (\sqrt{S} - 1) \quad , \quad (S > 1) \quad . \quad (31)$$

The above scenario for the initial banding kinetics is formally very similar to initial gas-liquid spinodal demixing kinetics as first described by Cahn and Hilliard [70, 71]. The equivalent of the shear-curvature viscosity is the square-gradient coefficient in the Cahn-Hilliard theory for spinodal decomposition. Similarly to the higher order derivative in the expression for the stress tensor, the Cahn-Hilliard square-gradient coefficient multiplies a higher order spatial derivative in Fick's diffusion equation, which accounts for the increase in the free energy on formation of sharp concentration gradients. The shear-curvature contribution to the stress tensor was introduced in Ref.[18] to describe gradient-banding. The stabilization of fast growth of large spatial gradients through the shear-curvature viscosity is a necessary feature for the numerical stability of algorithms to solve the above discussed equations of motion.

The stability criterion $S < 1$ in eq.(29) together with the explicit forms of the transport coefficients discussed before allows to construct the stability diagram. This diagram marks the combinations of shear rates and concentrations where the system turns from being (meta-)stable to unstable. There is an essential difference be-

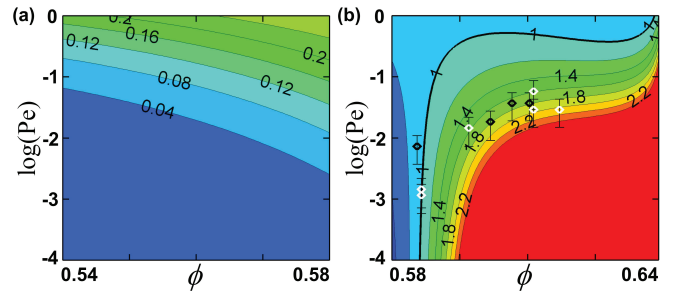


FIG. 6: The stability diagrams in the shear-rate versus concentration plane: (a) for $\phi < \phi_g$ and (b) for $\phi \geq \phi_g$. The thick line marks the transition from stable to unstable (where $S = 1$). The iso-S lines are indicated with their corresponding values for S , which curves are separated by a colour code (red is a relatively high value of S , blue a low value). The data points are experimental data for sterically stabilized PMMA particles: white data points are for particles with a radius of 138 nm, the black data points for 150 nm, taken from Ref.[41].

tween a system where the initial uniform volume fraction is smaller or larger than the glass-transition concentration ϕ_g . For $\phi < \phi_g$ we have $d\sigma/d\rho \sim \dot{\gamma}$, while for $\phi \geq \phi_g$, $d\sigma/d\rho \sim \text{constant}$ (for small Peclet numbers). This difference is due to the yield-stress contribution that is only present within the glass, and leads to a marked difference between the stability diagram for concentrations below and above the glass transition.

As can be seen from Fig.6a, for concentrations below the glass transition the uniform system is stable at least up to Peclet numbers of order 1. Within the glass, on the contrary, there is a large range of concentrations and relatively small shear rates where the uniform system is unstable. The thick solid line in Fig.6b marks the shear rates and concentrations where $S = 1$. This line marks the transition from the stable ($S < 1$) to unstable state ($S > 1$) of a uniform system.

The white and black data points in Fig.6b are experimentally determined transition points for PMMA spheres, taken from Ref.[41]. In view of our neglect of hydrodynamic interactions, these data compare reasonably well with theory.

As will be seen in section VI, banding can also occur for concentrations very close to the glass transition concentration without a SCC-instability. The stability criterion (29) is thus a sufficient but not a necessary condition for a stationary banded flow.

In the notation of Ref.[41], n is the exponent appearing in the shear-rate dependent stress for $\phi > \phi_g$. In our case $n = 1/2$ (the exponent $-1/2$ in the expression for the shear-rate dependent part of the viscosity, plus 1 as the viscosity is multiplied by the shear rate to obtain the stress). A similar value for $n \approx 0.4 - 0.5$ is adopted in Ref.[41]. The value for m in eqs.(18,19), which describes the shear-rate dependence of the osmotic pres-

sure, is chosen in eq.(5) of Ref.[41] to be slightly smaller than n . The resulting value $m = 0.4 - 0.5$ is similar to what we find in Fig.4c within the glass. The value of m , however, is found to be concentration dependent (see eq.(18)), varying from 0.50 for $\phi = \phi_g$ to 0.18 for $\phi = \phi_m$. The difference $m - n$ determines whether the $S = 1$ stability curve in the stability diagram in Fig.6b slopes to the left or to the right: for $m - n > 0$ the $S = 1$ curve has a negative slope, for $m - n < 0$ a positive slope. In the latter case the uniform glass becomes unstable on lowering the shear rate, which has been observed experimentally in Ref.[41]. Such a negative value of $m - n$ is also found in our analysis. The small difference between m and n leads to the essentially shear-rate independent location of the stability curve for the lower concentrations, as discussed in Ref.[41].

Note that eq.(5) for the pair-correlation function is only accurate for Peclet numbers typically less than unity. The SCC instability within the glass state indeed occurs at Peclet numbers smaller than unity, as can be seen from Fig.6b. For fluids, however, the instability occurs at most at quite high Peclet numbers, as can be seen from Fig.6a. To analyze the SCC instability below the glass transition requires therefore a representation of the pair-correlation function that is also accurate at much higher Peclet numbers, which is beyond the scope of the present study.

VI. NUMERICAL RESULTS FOR CONCENTRATION- AND FLOW-PROFILES

It has not been possible in previous work on colloids to calculate velocity and concentration profiles. There are no theoretical predictions yet concerning the velocity- and concentration profiles resulting from the SCC-instability. An essential ingredient for the calculation of velocity- and concentration profiles is the non-local contribution to the stress, as characterized by the shear-curvature viscosity, which stabilizes the system against arbitrary fast growth of variations/fluctuations with large spatial gradients. Without this non-local contribution to the stress any numerical algorithm would be inherently unstable.

To solve the non-linear differential equations, a 2^{nd} order central finite difference method is used to evaluate spatial derivatives, and a Newton-Rapson iteration is used to account for the non-linear term in Navier-Stokes equation, while the time derivative is determined using the predictor-corrector iteration scheme based on the Crank-Nicolson method (Adams method) [72]. In the numerical calculation, a spatial discretization is used that sets the maximum value of the wave vector k_{max} . When the number of grid points over an interval of length L is N_d , this maximum value of the wave vector is equal to $k_{max} = N_d\pi/L$. In case k_{max} is less than the critical wave vector k_c in eq.(30), not all unstable

Fourier modes are accounted for, and the numerical solutions are not realistic. A sufficiently fine grid must be chosen to assure that all unstable Fourier modes are accounted for. This is confirmed by comparing numerical solutions with a different number of grid points. In this simulation, $N_d = 200$ and $\tilde{dt} = 2 \times 10^{-3}$, while $N_d = 400$ and $\tilde{dt} = 5 \times 10^{-4}$ are used to verify convergence.

The two coupled equations of motion for the concentration and flow velocity as discussed in section IV will be solved numerically for a cylindrical Couette geometry (see Fig.7). Such a geometry features the inherent shear-gradients to induce the onset of the SCC-instability mechanism as explained in section II. All variables are assumed to be fully-developed in the θ -direction (around the cylinder axis), and homogeneous in the z -direction (along the cylinder axis). The only relevant spatial coordinate is therefore the radial distance from the cylinder axis, which will be denoted by r . The simulation domain in this direction is set by the radii R_1 and R_2 of the inner and outer cylinder, respectively. The gap width $R_2 - R_1$ is chosen as $1000a$ (with a the radius of the colloids), while $R_1/R_2 = 0.98$. As will be seen later, the spatial varying volume fraction deviates at most of the order of 0.005 around the initial uniform volume fraction, so that banded flow profiles can be calculated from numerical solutions of equations of motion by taking m in eq.(18) equal to its value corresponding to the initial volume fraction, independent of position. To verify this procedure, the additional contributions due to the concentration dependence of m to the equations of motion can be estimated from the numerical solutions using a constant m . These additional contributions turn out to be very small, which validates the use of a constant value for m .

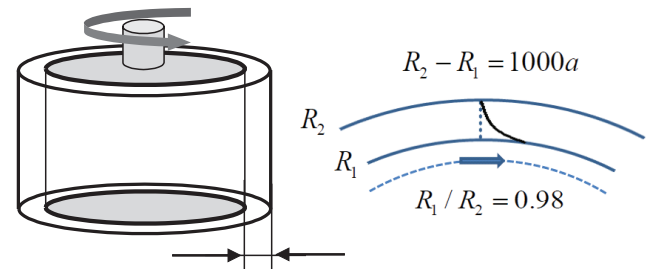


FIG. 7: The cylindrical Couette geometry. The radius of the inner, rotation cylinder is R_1 , the outer radius of the stationary cylinder is R_2 . The gap width is chosen to be 1000 times the radius a of the spherical colloids, and $R_1/R_2 = 0.98$.

The equation of motion for the concentration in terms of the radial cylindrical coordinate reads,

$$\frac{\partial \rho(r, t)}{\partial t} = \frac{1}{r} \frac{\partial}{\partial r} \left\{ r D_{eff} \frac{\partial \rho(r, t)}{\partial r} \right\} + \frac{1}{r} \frac{\partial}{\partial r} \left\{ r \xi \frac{\partial \dot{\gamma}(r, t)}{\partial r} \right\}.$$

The stress is the sum of the yield-stress and a viscous-

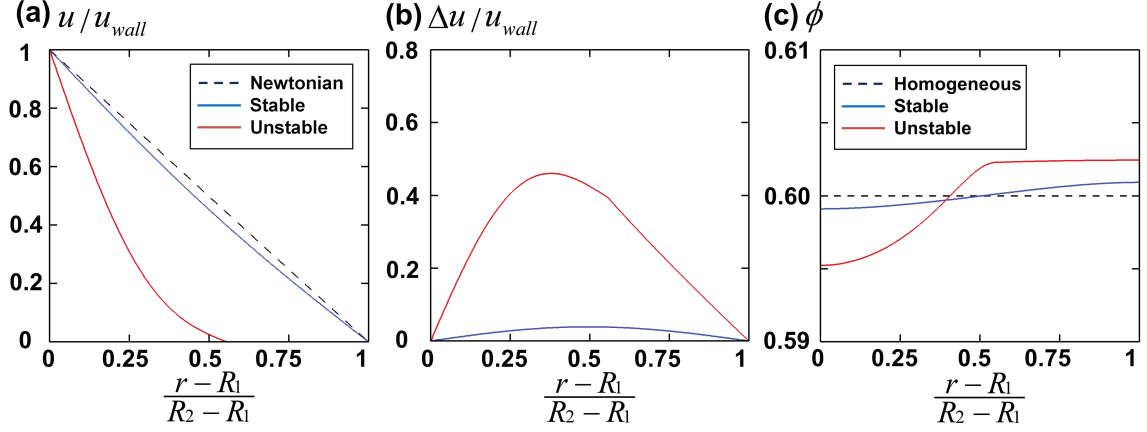


FIG. 8: Stationary profiles for a volume fraction of 0.60, well within the glass. (a) Velocity profiles: the dashed blue curve is for a Newtonian fluid, the blue solid line for a stable initial state where the applied dimensionless stress is equal to 200, and the red solid curve for an unstable initial state with an applied stress equal to $\tilde{\Sigma}(R_1) = 50$. The corresponding Peclet numbers are 1.0 and 0.0078, respectively. Velocities are normalized with respect to the velocity of u_{wall} of the rotating inner cylinder. (b) The difference of the flow velocity of a Newtonian fluid and the local velocity. (c) The position dependent volume fraction.

stress contribution,

$$\Sigma = \Sigma_{yield} + \Sigma_{visc} ,$$

where the yield stress is given in eq.(23), while,

$$\Sigma_{visc} = \left(\eta - \kappa \frac{1}{r} \frac{\partial}{\partial r} \left\{ r \frac{\partial}{\partial r} \right\} \right) \dot{\gamma}(r, t) .$$

The Navier-Stokes equation reads,

$$\frac{\partial}{\partial r} \{ r^2 \Sigma \} = 0 ,$$

provided that the total local stress is larger than the yield stress. No-slip is assumed at both the walls of the inner and outer cylinder, that is, the suspension flow velocity is zero at the stationary outer wall where $r = R_2$, and equal to the non-zero wall velocity of the inner wall for $r = R_1$. The applied stress at the rotating inner cylinder will be fixed. There is no principle difference between controlled stress and controlled shear-rate experiments (contrary to gradient-banding in the absence of coupling to concentration, where banding does not occur under controlled stress conditions). The applied stress is hereafter specified by the dimensionless stress,

$$\tilde{\Sigma}(R_1) = \frac{\Sigma(r = R_1)}{k_B T / a^3} . \quad (32)$$

There are no mass fluxes through the walls of both cylinders: $j(R_1) = 0 = j(R_2)$. Due to the inclusion of the shear-curvature contribution we need a third set of boundary conditions. As the gap width is relatively small compared to the inner cylinder radius, so that

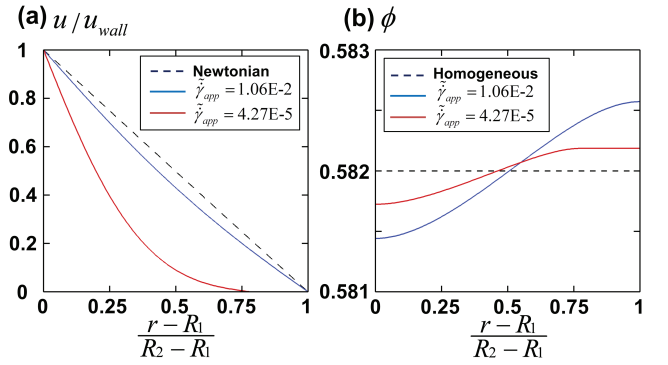


FIG. 9: Stationary profiles starting from a stable state, for a concentration just above the glass transition, for an overall volume fraction of $\phi = 0.582$. (a) The velocity profile and (b) the volume fraction, for applied stresses of $\tilde{\Sigma}(R_1) = 14$ (the red curves) and 20 (the blue curves). The resulting apparent Peclet numbers $\tilde{\gamma}$ are indicated in the figure. Velocities are normalized by the velocity of the rotating inner cylinder u_{wall} . The black dashed line is the profile for a Newtonian fluid.

variations of the shear rate are relatively small in the non-banded state, we use here as the third boundary condition that the shear rates are constant in the vicinity of the walls: $\partial \dot{\gamma}(r, t) / \partial r = 0$ for both $r = R_1$ and $r = R_2$.

The remaining parameter that needs to be specified is the shear-curvature viscosity κ_0 . The interface thickness in a stationary shear-banded state is of the order

$\sqrt{\kappa_0/\eta_0}$, so that the dimensionless quantity,

$$\tilde{\Lambda} = \frac{1}{a} \sqrt{\frac{\kappa_0}{\eta_0}},$$

is a measure for the interface thickness in units of the radius a of the colloids. The interface thickness is probably much larger than the size of the colloids, so that we will use $\tilde{\Lambda} = 100$ in the numerical analysis.

Stationary flow- and concentration-profiles for an initially homogeneous state are given in Fig.8. The initial overall concentration is 0.60, which well within the glass. The dashed line in Fig.8a is the flow profile for pure solvent, and the solid blue line corresponds to an initially stable suspension with an applied dimensionless stress at R_1 of $\tilde{\Sigma}(R_1) = 50$ (see eq.(32)), while the red curve corresponds to an initially unstable state with a dimensionless stress of 200. The velocities are normalized with respect to the velocity u_{wall} of the inner cylinder. The Newtonian velocity profile is essentially linear for the small gap width under consideration. The stable flow profile is somewhat curved, which is due to the shear-gradient induced mass flux. For the initially unstable state the final flow profile (the red curve in Fig.8a) exhibits a banded structure, where one band is non-flowing. The self-amplified mass flux leads to an increase of the concentration near the outer cylinder to an extent that the local yield stress becomes larger than the local applied stress, leading to an arrest of the local flow. The slight curvature within the flowing band near the non-flowing band is related to the width of the interface which is set equal to a tenth of the total gap width. In Fig.8b the difference between the velocity of a Newtonian fluid and the local velocity is plotted. The stationary concentration profiles are given in Fig.8c. As can be seen, the variation of the concentration around the overall concentration is limited to about 0.01, which justifies to use the value of the exponent m corresponding to the overall concentration. That small changes in concentration are sufficient to induce a banded flow is due to the strong concentration dependence of transport coefficients and viscometric functions.

Banded flows can also occur for initially stable systems. For an overall concentration of 0.582 and an applied dimensionless stress of $\tilde{\Sigma}(R_1) = 14$, the stability parameter is always around 0.6. It is never larger than unity, not in the initial state nor in the transient states. Nevertheless we find a banded structure with very much the same features as the banded flow profile in case of a SCC-instability, as can be seen in Fig.9a (the red curve). The banded flow is now not due to the SCC-instability. The stability criterion discussed in section V is thus a sufficient but not a necessary condition for banding. The reason for banding in this case is as follows. The local dimensionless stress at the outer cylinder is 13.446. This is just above the yield stress of 13.440 for the initial concentration. The shear-

induced mass flux towards the outer cylinder, without self-amplification, is now sufficient to increase the local concentration to a value that leads to a local yield stress that is larger than the local stress, so that the local velocity vanishes, resulting in a banded flow profile. The slight increase in concentration at the outer cylinder is illustrated in Fig.9b (the red curve). For the small increase of the concentration that is necessary to lower the local stress at the outer cylinder below the yield stress, there is no need for the self-amplifying increase of concentration. For larger initial concentrations, the SCC-self-amplification mechanism is necessary to give rise to a sufficiently large increase of the local concentration such that the local yield stress becomes larger than the actual local stress at the outer cylinder. The blue curves in Figs.9a,b are for a larger applied dimensionless stress of 20. For this relatively high applied stress, the local stress is always larger than the local yield stress so that there is no banding. As before, the curvature of the flow profile is now entirely due to the shear-curvature contribution to the stress.

It is in principle possible that in part of the system the concentration is above, and in part below the glass-transition concentration. This only happens when the initial volume fraction is to within about 0.001 in the vicinity of the glass-transition concentration, and is therefore hardly of experimental relevance. A numerical solution for such cases would also require an entirely new computer algorithm in order to match the regions where the concentration is above and below the glass-transition concentration. We therefore refrain from an analysis of this rather esoteric situation.

In analogy with thermodynamically driven phase transitions in the absence of flow, spinodals and binodals can be defined in case of banding transitions [19, 20]. The spinodal is generally defined as the points where the system becomes unstable (this is the line where $S = 1$ in Fig.6b). As banding can also occur outside the unstable region where $S > 1$, as seen above, one might define the region where $S < 1$ but nevertheless banding occurs, as the meta-stable region, which is bounded by the binodal. Contrary to gradient-banding, however, the location of the binodal is not an intrinsic property of the system under consideration, but also depends on the shear-cell geometry. For example, when the gap width of a Couette is increased, the natural spatial gradients in the shear rate are increased, which increases the shear-gradient induced mass flux, so that banding of the SCC type for hard-sphere glasses occurs down to lower concentrations. The binodal thus shifts to lower concentrations as the cell gap width is increased.

The temporal evolution of the flow and concentration profiles of the unstable system, for which stationary profiles were given in Fig.8, are shown in Fig.10. The initial condition here is a spatially constant concentration. The stability factor in the initial state is equal to

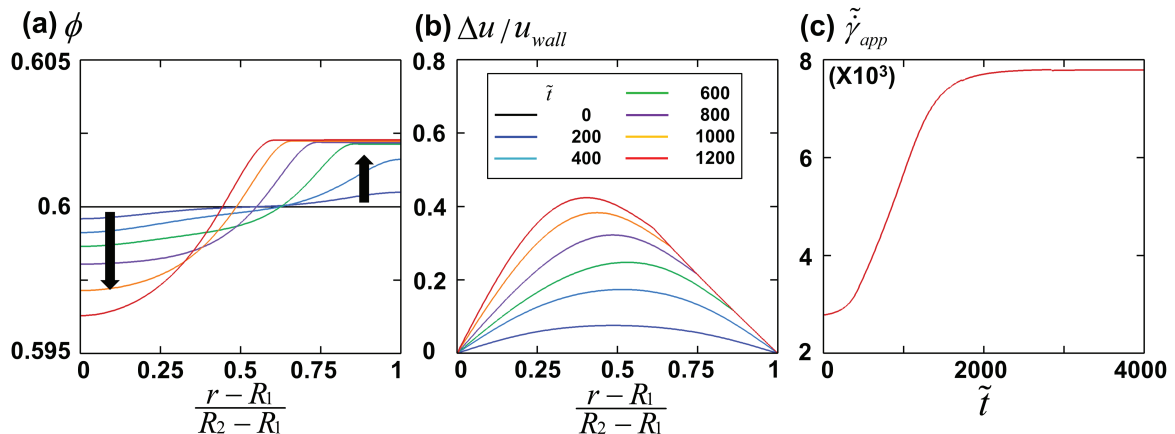


FIG. 10: Temporal evolution of (a) the concentration profile, (b) of the velocity profile, and (c) of the apparent Peclet number. The various times $\tilde{t} = t D_0 / a^2$ are indicated in (b). The overall volume fraction of 0.60, and the applied stress of $\tilde{\Sigma}(R_1) = 50$, of which the stationary profiles are given in Fig.8, the red curves). Video's can be found in the supplementary material.

1.00077 and 1.00540, at $r = R_2$ and $r = R_1$, respectively. The typical wave length $2\pi/k_m$ of the (position dependent) most rapidly growing Fourier component is thus found from eq.(31) to be of the order of the gap width. This explains the smooth growth of the profiles in Fig.10a,b. Similar smooth growth kinetics is found in the experiments in Ref.[41]. As the applied stress is fixed, the overall shear rate changes during band formation. This apparent Peclet number is plotted in Fig.10c. The temporal increase of the shear rate shows that the viscosity of the suspensions as a whole decreases during banding. The video "Video-SCC-1" in the supplementary information shows the temporal evolution of the suspension flow velocity and the volume fraction.

For the initial conditions in the above examples, a spatially uniform density has been chosen. An at randomly chosen initial condition for the concentration (and hence the corresponding flow velocity), as a superposition of Fourier modes with wavelengths up to the gap width, leads to the same final state as for the uniform initial state. Higher order Fourier modes decay fast, while the smooth variations slowly grow very much as for the uniform initial state. This is due to the value of the stability factor S , which is close to unity, so that according to the discussion in section 6 only smooth spatial variations are unstable. The video "Video-SCC-2" in the supplementary information shows the temporal evolution of the flow velocity and the volume fraction up to $\tilde{t} = 700$ for three different initial conditions.

VII. SUMMARY AND CONCLUSIONS

An essential ingredient for the Shear-gradient Concentration Coupling (SCC-) instability is a mass flux

that is induced by spatial gradients of the shear rate. The microscopic origin of this mass flux is elucidated, and it is shown that the force that drives the mass flux is related to gradients of a "generalized osmotic pressure" that is formally equal to the standard expression for the equilibrium osmotic pressure, but where the pair-correlation function is now the shear-distorted pair-correlation function. This result leads to expressions for the transport coefficients that enter the advection-diffusion equation in terms of the shear-distorted pair-correlation function.

Brownian Dynamics (BD-) simulations are performed for concentrated hard-sphere suspensions under shear flow to obtain the shear-distorted pair-correlation function, and thereby explicit expressions for the shear-rate and concentration dependence of these transport coefficients. The advection-diffusion equation is coupled to the Navier-Stokes equation, for which accurate expressions for the concentration dependence of the viscosity and the yield stress as known from the literature are adopted.

Essential is the inclusion of a non-local stress contribution, the "shear-curvature stress", which stabilizes the system against the arbitrary fast growth of large spatial gradients of the flow velocity.

The coupled advection-diffusion and Navier-Stokes equations are used to construct stability diagrams. Numerical solutions of these coupled equations for a Couette geometry allow us to study the banded concentration- and velocity-profiles. For the hard-sphere system under consideration it is found that banded flow profiles occur for concentrations above the glass concentration within a large part of the shear-rate versus concentration plane. The SCC-instability is predicted to occur at very low shear rates, in accordance

with experiments. One of the bands has a very small shear rate, and is essentially non-flowing. Outside the interface connecting the two bands, the shear rate is essentially constant, independent of position within the flowing band. There is a weak spatial variation of the shear rate due to the shear-curvature contribution to the stress.

It should be noted that the kinetics of shear-band formation as well as the final stationary state of SCC-banded structures depends on the shear-gradients that are naturally present in the shear-geometry that is used in an experiment. For example, there is most likely a difference concerning the SCC-characteristics in a Couette cell as compared to a cone-plate geometry where secondary flow determines the shear-gradient induced mass transport.

Banding is also found to occur without the SCC-instability, provided that the concentration is very close to the glass transition. In such cases the mass flux need not be self-amplified in order that the locally applied stress becomes less than the local yield stress, which leads to banding. The mere geometry-imposed shear-gradient induced mass flux is sufficient to increase the local density by the small amount needed to induce a yield stress that is larger than the locally applied stress.

For larger concentrations, deeper into the glass, self-amplification of the mass flux is necessary to achieve this.

In this work we neglected hydrodynamic interactions between the colloidal particles. The above work could be improved by including hydrodynamic interactions, which affect the shear-rate and concentration dependence of the transport coefficients that enter the advection-diffusion equation. A second improvement would be to include elastic contributions to the stress, which might affect banding kinetics.

Acknowledgments

We are grateful to M.E. Cates and W.C.K. Poon (both authors in Ref.[41]) for their useful comments and for providing us with the experimental data that are given in the stability diagram in Fig.6. K.H. Ahn acknowledges the support from the National Research Foundation of Korea (NRF) grant (No. 2013R1A2A2A07067387) funded by the Korea government (MEST).

-
- [1] P.D. Olmsted, *Current Opinion in Colloid and Interface Science*, 1999, **4**, 95.
- [2] J. Vermant, *Current Opinion in Colloid and Interface Science*, 2003, **6**, 489.
- [3] J.-F. Berret, in *Molecular Gels* (eds. Weiss RG, Terech P), *Rheology of wormlike micelles : Equilibrium properties and shear banding transition*, Springer, Dordrecht, 2005, 235.
- [4] M.E. Cates, S.M. Fielding, *Adv. Phys.*, 2006, **55**, 799.
- [5] P.T. Callaghan, *Rheol. Acta*, 2008, **47**, 243.
- [6] J.K.G. Dhont, W.J. Briels, *Rheol. Acta*, 2008, **47**, 257.
- [7] P.D. Olmsted, *Rheol. Acta*, 2008, **47**, 283.
- [8] S. Manneville, *Rheol. Acta*, 2008, **47**, 301.
- [9] T.C.B. McLeish, R.C. Ball, 1986 *J. Polym. Sci.*, 1986, **24**, 1735.
- [10] T.C.B. McLeish, *J. Polym. Sci.*, 1987, **25**, 2253.
- [11] A.W. El-Kareh, L.G. Leal, *J. Non-Newtonian Fluid Mech.*, 1989, **33**, 257.
- [12] N.A. Spenley, X.F. Yuan, M.E. Cates, *J. Phys. II (France)*, 1996, **6**, 551.
- [13] X.-F. Yuan, *Europhys. Lett.*, 1999, **46**, 542.
- [14] O. Radulescu, P.D. Olmsted, C.-Y. D. Lu, *Rheol. Acta*, 1999, **38**, 606.
- [15] P.D. Olmsted, O. Radulescu, C.-Y. D. Lu, *J. Rheol.*, 2000, **44**, 257.
- [16] O. Radulescu, P.D. Olmsted, *J. Non-Newtonian Fluid Mech.* 2000, **91**, 141.
- [17] O. Radulescu, P.D. Olmsted, J.P. Decruppe, S. Lerouge, J.-F. Berret, G. Porte, *Europhys. Lett.*, 2003, **62**, 230.
- [18] J.K.G. Dhont, *Phys. Rev. E*, 1999, **60**, 4534.
- [19] P.D. Olmsted, C.-Y.D. Lu, *Phys. Rev. E*, 1997, **56**, 55.
- [20] P.D. Olmsted, C.-Y.D. Lu, *Phys. Rev. E*, 1999, **60**, 4397.
- [21] J.L. Goveas, P.D. Olmsted, *Europhys. Phys. J. E*, 2001, **6**, 79.
- [22] K. Kang, M.P. Lettinga, Z. Dogic, J.K.G. Dhont, *Phys. Rev. E*, 2006, **74**, 026307.
- [23] M.A. Fardin, T.J. Ober, C. Gay, G. Grégoire, G.H. McKinley, S. Lerouge, *Europhys. Phys. J.*, 2011, **96**, 4404.
- [24] M.A. Fardin, B. Lasne, O. Cardoso, G. Grégoire, M. Argentina, J.P. Decruppe, S. Lerouge. *Phys. Rev Lett.*, 2009, **103**, 028302.
- [25] S. Lerouge, M. Argentina, J.P. Decruppe, *Phys. Rev. Lett.*, 2006, **96**, 088301.
- [26] S.M. Fielding, *Phys. Rev. E*, 2007, **76**, 016311.
- [27] M.A. Fardin, D. Lopez, J. Croso, G. Grégoire, O. Cardoso, G.H. Mckinley, S. Lerouge, *Phys. Rev. Lett.*, 2010, **104**, 178303.
- [28] P.D. Olmsted, *Eur. Phys. Lett.*, 1999, **48**, 339.
- [29] S.M. Fielding, P.D. Olmsted, *Eur. Phys. J. E*, 2003, **11**, 65.
- [30] A. Onuki, *J. Phys. Soc. Jpn.*, 1990, **59**, 3423.
- [31] S.T. Milner, *Phys. Rev. E*, 1993, **48**, 3691.
- [32] H. Ji, E. Helfand, *Macromolecules*, 1995, **28**, 3869.
- [33] S.T. Milner, *Phys. Rev. E*, 1993, **48**, 3674.
- [34] S.T. Milner, in *Theoretical Challenges in the Dynamics of Complex Fluids* (ed. T.C.B McLeish), *Effects of shear flow on semidilute polymer solutions*, Kluwer Academic Publishers, The Netherlands, 1997, 127.
- [35] M. Cromer, M.C. Villet, G.H. Fredrickson, L.G. Leal, R. Stepanyan, M.J.H. Bulters, *J. Rheol.*, 2013, **57**, 1211.

- [36] S. Mandal, M. Gross, D. Raabe, F. Varnik, *Phys. Rev. Lett.*, 2012, **108**, 098301.
- [37] P. Nozieres, D. Quemada, *Europhys. Lett.*, 1986, **2**, 129.
- [38] V. Schmitt, C.M. Marques, F. Lequeux, *Phys. Rev. E*, 1995, **52**, 4009.
- [39] B. Garcia-Rojas, F. Bautista, J.E. Puig, O. Manero, *Phys. Rev. E*, 2009, **80**, 036313.
- [40] M. Cromer, M.C. Villet, G.H. Fredrickson, L.G. Leal, *Physics of Fluids*, 2013, **25**, 051703.
- [41] R. Besseling, L. Isa, P. Ballesta, G. Petekidis, M. E. Cates, and W. C. K. Poon, *Phys. Rev. Lett.* 2010, **105**, 268301.
- [42] J.F. Morris, F. Boulay, *J. Rheol.*, 1999, **43**, 1213.
- [43] Y. Yurkovetsky, J.F. Morris, 2008, **52**, 141.
- [44] A. Deboeuf, G. Gauthier, J. Martin, Y. Yurkovetsky, J.F. Morris, *Phys. Rev. Lett.*, 2009, **102**, 108301.
- [45] D.R. Foss and J.F. Brady, *J. Rheol.*, 2000, **44**, 629.
- [46] P.R. Nott, J.F. Brady, *J. Fluid Mech.*, 1994, **275**, 157.
- [47] D. Leighton, A. Acrivos, *J. Fluid Mech.*, 1987, **181**, 415.
- [48] A. Acrivos, G.K. Batchelor, E.J. Hinch, D.L. Koch, R. Mauri, *J. Fluid Mech.*, 1992, **240**, 651.
- [49] J.K.G. Dhont, K. Kang, M.P. Lettinga, W.J. Briels, *Korea-Australia Rheology Journal*, 2010, **22**, 291.
- [50] D.S. Wogerere, J.F. Morris, E.R. Weeks, *J. Fluid Mech.*, 2007, **581**, 437.
- [51] D.A. McQuarrie, *Statistical Mechanics*, Harper & Row Publishers, 1973 (page 282).
- [52] J.K.G. Dhont, *An Introduction to Dynamics of Colloids*, Elsevier, 1996 (page 472).
- [53] D.M. Heyes, J.R. Melrose, *J. Non-Newtonian Fluid Mech.*, 1993, **46**, 1.
- [54] N.F. Carnahan, K.E. Starling, *J. Chem. Phys.*, 1969, **51**, 635.
- [55] M.D. Rintoul, S. Torquato, *J. Chem. Phys.*, 1996, **105**, 9258.
- [56] C.G. de Kruif, E.M.F. van Iersel, A. Vrij, W.B. Russel, *J. Chem. Phys.*, 1985, **83**, 4717.
- [57] G.N. Choi, I.M. Krieger, *J. Coll. Int. Sci.*, 1986, **113**, 101.
- [58] J.C. van der Werff, C.G. de Kruif, *J. Rheol.*, 1989, **33**, 421.
- [59] R. A. Lionberger, *J. Rheol.*, 1998, **42**, 843.
- [60] D.R. Foss, J.F. Brady, *J. Fluid Mech.*, 2000, **407**, 167.
- [61] G. Petekidis, D. Vlassopoulos, P.N. Pusey, *J. Phys.: Condens. Matter*, 2004, **16**, S3955.
- [62] Z. Cheng, J. Zhu, P.M. Chaikin, S.-E. Phan, W.B. Russel, *Phys. Rev. E*, 2002, **65**, 041405.
- [63] A.J. Banchio, J. Bergenholtz, G. Nägele, *Phys. Rev. Lett.*, 1999, **82**, 1792.
- [64] A.J. Banchio, G. Nägele, J. Bergenholtz, 1999, **111**, 8721.
- [65] I.M. Krieger, *J. Coll. Int. Sci.*, 1972, **3**, 111.
- [66] E.J. Saltzman, K.S. Schweizer, *J. Chem. Phys.*, 2003, **119**, 1197.
- [67] J. Goyon, A. Colin, G. Ovarlez, A. Ajdari, L. Bocquet, *Nature*, 2008, **454**, 84.
- [68] K.N. Pham, G. Petekidis, D. Vlassopoulos, S.U. Egelhaaf, W.C.K. Poon, P.N. Pusey, *J. Rheol.*, 2008, **52**, 649.
- [69] A. Ikeda, L. Berthier, *Phys. Rev. E*, 2013, **88**, 052305.
- [70] J.W. Cahn, J.E. Hilliard, *J. Chem. Phys.*, 1958, **28**, 258.
- [71] J.W. Cahn, J.E. Hilliard, *J. Chem. Phys.*, 1959, **31**, 688.
- [72] Parviz Moin, *Fundamentals of Engineering Numerical Analysis 2e/*, 2010; Cambridge University Press, Cambridge.